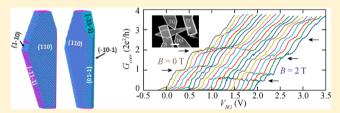# Twin-Induced InSb Nanosails: A Convenient High Mobility Quantum System

María de la Mata,[†] Renaud Leturcq,[*,‡,§] Sébastien R. Plissard,[∥] Chloé Rolland,[‡] César Magén,[⊥] Jordi Arbiol,[*,†,#] and Philippe Caroff[*,‡,∇]

[†]Catalan Institute of Nanoscience and Nanotechnology (ICN2), CSIC and The Barcelona Institute of Science and Technology, Campus UAB, Bellaterra, 08193 Barcelona, Spain

[‡]Institut d'Électronique, de Microélectronique et de Nanotechnologie, UMR CNRS 8520, Avenue Poincaré, C.S. 60069, 59652 Villeneuve d'Ascq, France

[§]Materials Research and Technology (MRT) Department, Luxembourg Institute of Science and Technology (LIST), 5, avenue des Hauts-Fourneaux, L-4362 Esch-sur-Alzette, Luxembourg

[∥]CNRS-Laboratoire d'Analyse et d'Architecture des Systèmes (LAAS), Université de Toulouse, 7 avenue du colonel Roche, 31400 Toulouse, France

[⊥]Laboratorio de Microscopías Avanzadas (LMA), Instituto de Nanociencia de Aragon (INA) -ARAID, and Departamento de Física de la Materia Condensada, Universidad de Zaragoza, 50018 Zaragoza, Spain

[#]Institució Catalana de Recerca i Estudis Avançats (ICREA), 08010 Barcelona, Catalonia, Spain

[∇]Department of Electronic Materials Engineering, Research School of Physics and Engineering, The Australian National University, Canberra, ACT 0200, Australia

S Supporting Information

ABSTRACT: Ultra narrow bandgap III−V semiconductor nanomaterials provide a unique platform for realizing advanced nanoelectronics, thermoelectrics, infrared photodetection, and quantum transport physics. In this work we employ molecular beam epitaxy to synthesize novel nanosheet-like InSb nanostructures exhibiting superior electronic performance. Through careful morphological and crystallographic character-ization we show how this unique geometry is the result of a single twinning event in an otherwise pure zinc blende structure. Four-terminal electrical measurements performed in both the Hall and van der Pauw configurations reveal a room temperature electron mobility greater than 12 000 cm^2·V^{-1}·s^{-1}. Quantized conductance in a quantum point contact processed with a split-gate configuration is also demonstrated. We thus introduce InSb "nanosails" as a versatile and convenient platform for realizing new device and physics experiments with a strong interplay between electronic and spin degrees of freedom.

KEYWORDS: III−V semiconductor, nanowires, molecular beam epitaxy, Hall measurements, quantum point contact, Cs-corrected scanning transmission electron microscopy

High-quality narrow bandgap III−V semiconductor nano-structures hold promise for applications in infrared optoelectronics,[1,2] low-power nanoelectronics,[3,4] and quantum physics.[5] Until now, reports have focused on the nanowire geometry which has been used to demonstrate direct integration on silicon,[6] gate-all-around (tunnel) field effect transistors,[7−9] efficient IR photodetection,[10,11] lasing[12−14] and enhanced thermoelectric performance.[15−20]

With the narrowest bandgap among the III−V semi-conductors, InSb is characterized by an extremely low effective carrier mass and therefore has the potential to realize some of the highest values of electron mobility among all semi-conductors. Coupled with the largest Landé g-factor of all semiconductors[21] and the fact that peak electron velocity occurs at relatively low electric fields, InSb is an ideal material

for high speed and low power nanoelectronics[22] and 0D/1D electron or hole systems for quantum transport physics.[23−25] High-quality InSb nanowires have already been shown to enable fast manipulation of spin−orbit qubits[24,26] and have played a key role in the search for the elusive Majorana fermion.[27−29]

The epitaxial growth conditions and crystal quality of antimonide nanostructures differ significantly from those of all other III−Vs due to both the low vapor pressure of Sb and its action as a surfactant.[30] On one hand, these specificities make growth of InSb free-standing nanostructures challenging
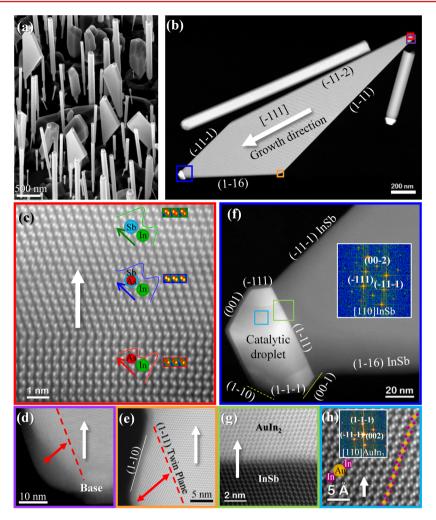
Figure 1. General morphology and crystal structure. (a) SEM image (30° tilt) showing a representative overview of an as-grown InAs/InSb ensemble containing nanosails. (b) Low magnification HAADF image of a nanosail with the regions magnified in c–h indicated by colored squares. (c) Atomic resolution HAADF image of the base of the nanosail (growth direction is vertical) showing both WZ InAs and ZB InSb. Red, blue, and green curves correspond to intensity profiles taken along individual dumbbells in order to determine polarity, which was found to be B-polar for both InAs and InSb. (d,e) High resolution images of the twin boundary extending parallel to the {111} lateral facet, from the base (d) to its termination (e), where the twinned segment is of constant width (highlighted by the red arrow). (f) Z-contrast image of the nanosail's tip, showing the facets of the AuIn$_2$ seed particle. A fast Fourier transform (FFT) of the InSb nanosail structure is inset. (g) Atomically resolved image of the interphase between the InAs nanosail structure (darker) and the AuIn$_2$ single crystalline seed particle (brighter). (h) Atomic resolution image of the AuIn$_2$ structure with FFT inset. Note that the white arrow points indicate the [$\bar{1}$11] growth direction.

due to the necessity of providing nanowire "stems" to nucleate them away from the substrate,[31] impractically slow growth rates in the axial direction,[32] and the existence of very narrow "sweet spot" in the growth parameter space.[33] On the other hand, these special growth conditions guarantee a perfect crystal structure independently of the growth technique,[34−37] a total absence of tapering for nanowires thanks to a very low nucleation probability on their {110} sidewalls, and the opportunity to tailor the morphology, to deliver geometries such as diamond-shaped free-standing 3D nanostructures[33,38] or nanocrosses.[39,40] While antimonide nanocrystals usually lack planar defects perpendicular to the growth direction, the appearance of crystallographic defects in other directions can induce changes in the geometry of the overall system rather than promoting a crystal phase transition, explaining the formation of tilted nanowires,[41] branched nanostructures,[42] or kinking phenomena.[43] Despite these achievements, the nanowire geometry has proven impractical for the realization of multiterminal devices such as Hall bars,[44,45] quantum point

contacts, or Aharonov-Bohm rings.[46] Realizing nanosheets of this material while keeping the advantages already demonstrated by nanowires would thus open the way to more advanced device geometries[47] and still enable advanced heterostructures,[48] while also significantly easing the device fabrication process.[49] There are currently however few reports of free-standing III−V nanosheets, and the majority of these examples contain at least a few stacking defects perpendicular to their vertical growth axis.[50−54]

Here we show that InSb nanosheets in the form of a vertical nanosail can be grown epitaxially from an InAs "mast" acting as a stem, with a thickness controlled by the seed particle, two large atomically flat {110} surfaces, and a highly faceted geometry. Growth is possible using the two main epitaxy techniques, i.e., metal−organic vapor phase epitaxy (MOVPE) and molecular beam epitaxy (MBE), but only the latter is detailed here. The nanosail crystal structure grown by MBE is confirmed to be pure zinc blende with only a single isolated twin boundary event on the lateral side. It is found that the
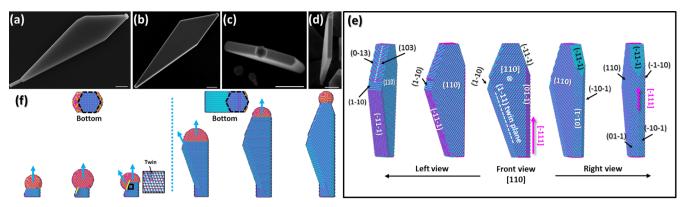
Figure 2. 3D facet structure and growth scenario. (a–d) Various SEM images of nanosails either lying flat on a silicon host substrate (a,b) or free-standing (c,d), revealing the general geometry and small variations in shape. Scale bars are 200 nm for a−d. (e) Atomic 3D model of the nanosail illustrating its main facets and geometry. (f) Evolution of the nanosail geometry.

single twin drives the crystal to change its geometry and expand to create the observed 2D-like morphology. We then proceed with studying its key electronic figures of merit such as mobility and carrier concentration using a multiterminal device configuration. A very high mobility above 12 000 cm$^2 \cdot$V$^{-1} \cdot$s^{-1} is unambiguously determined both at low temperature and room temperature. Finally, we demonstrate for the first time quantized conductance in a bottom-up InSb nanomembrane in a quantum point contact (QPC),[55,56] in the absence of an in-plane applied magnetic field.[57]

The InAs/InSb nanowire/nanosail heterostructures were grown on InP (111)B via a gold-assisted vapor−liquid−solid mechanism in a Riber 32-P gas-source molecular beam epitaxy (MBE) system following a methodology very similar to that reported by Thelander et al.[37] The structure consists, from bottom to top, of a short InP/InAs stem followed by the InSb segment. The general morphology and faceting was evaluated using a Zeiss Ultra 55 SEM, while mechanically detached nanostructures were studied by atomic resolution high angle angular dark-field scanning transmission electron microscopy (HAADF-STEM) using a probe corrected FEI Titan 60-300 equipped with a high brightness field emission gun (XFEG) and a CETCOR corrector from CEOS. All of the 3D atomic models presented here have been created using the Rhodius software.[58,59] Back-gated devices where fabricated by transferring the nanosails onto a thermally oxidized highly doped Si substrate. Low resistive ohmic contacts were then defined by electron beam lithography on ammonium sulfide passivated nanostructures. For the quantum point contact (QPC) device, two ohmic contacts are realized, followed by the deposition of a 10 nm HfO$_2$ conformal gate dielectric layer by atomic layer deposition, and two split gates defined by electronic lithography. Variable temperature magneto-transport experiments were performed in a helium cryostat with a variable temperature insert allowing measurements from 2.1 to 300 K and a magnetic field up to 7 T. The Hall and van der Pauw measurements were performed using the lock-in technique. The quantum point contact measurements were performed with a constant d.c. bias voltage. Full growth, characterization, and processing details are given in Supporting Information (Section SA).

Figure 1a presents an as-grown InAs/InSb nanowire ensemble containing nanosails structures. Growth here consisted of axial InP/InAs heterostructure stems topped with an InSb segment. Only the bottom InAs stem and InSb

sections are visible in this scanning electron microscopy (SEM) image. It is clear that, while some InAs/InSb heterostructures remain in the shape of standard nanowires[35] or even diamond-shaped crystallites,[33,38] a significant proportion of the InSb segments form flat sail-like nanosheets, which we henceforth refer to as "nanosails". The variation observed here may be related to the stochastic nature of the Au dewetting process which produces a distribution of seed diameters and areal densities and the extreme sensitivity of free-standing InSb nanostructures to local growth conditions.[31−33] An illustration of this intrinsic sensitivity of InSb to local growth conditions is illustrated in Supporting Figure S1. It can therefore be inferred that the specific nucleation event leading to this original InSb nanosail morphology has a small probability of occurrence under the studied growth conditions. The percentage of nanosails to nanowires is measured to be 5.6% (see Supporting Figure S3). The ease of obtaining the nanosail geometry is further confirmed in Supporting Figure S2 where the same nanostructures are grown by MOVPE (see Supporting Figure S2).

After mechanical dispersion on a holey carbon grid, the nanosails facets were indexed using atomically resolved high angle annular dark field (HAADF) scanning transmission electron microscopy (STEM). The primary facets were determined to be {110} type bordered mostly by {111} type facets (Figure 1b). Considering the base of the nanosail, Figure 1c, we observe that the narrow InAs "mast" segment below the InSb section crystallizes in the wurtzite (WZ) structure, while the rest of the sail (composed of pure InSb) presents a pure zinc-blende (ZB) structure (Figure 1c). The polarity of the growth direction is further confirmed to be anionic or "B" type by measuring the intensity profile along dumbbells (colored curves in Figure 1c).[60] This analysis also reveals the presence of As in the first nanometers of the InSb ZB base. Indeed the relative intensity inversion observed (i.e., InAs shows As polarity, with In the heavier constituent (red plot in Figure 1c), while InSb presents Sb polarity being Sb the heavier (green plot in Figure 1c) which demonstrates that the interface between materials is not abrupt, as reported previously for InAs/InSb nanowires.[61] Further strain analysis shown in Supporting Figure S4 along with EELS measurements confirm the alloying at the InAs/InSb interface over a few nanometers. Focusing now on the InSb nanosail itself, all investigated samples were characterized by a pristine ZB structure with the exception of a single longitudinal twin boundary located at the base (see

Figure 1e) and extending parallel to one of the {111} lateral facets of the structures, disappearing at the corner (Figure 1f) where the new facet shrinking the structure starts to develop. This single structural defect will be discussed in details in the following and in Supporting Information.

Postgrowth, the seed particles were found to be single $AuIn_2$ crystals with a cubic $Fm3\text{-}m$ structure (Figure 1g,h) and perfectly lattice-matched to the nanosail: $(-11-1)$ $[110]$ $AuIn_2$ $\parallel$ $(-111)[110]$ InSb. The $AuIn_2$ composition is in agreement with the pseudo binary eutectic region of the Au−In−Sb ternary phase diagram, as discussed in previous works.[35,36,62] The interface between the sail and the alloy metal particle is atomically flat, and there is no evidence of gold diffusion within the nanosail structure. The particle exhibits low-index facets, as shown Figure 1d, similar to those previously reported for InSb NWs.[61]

Having established that our nanostructures were of the highest crystalline quality, we then further investigate their faceting and 3D geometry using both experimental data and 3D atomistic modeling. From the analysis of a combination of SEM images taken with both titled view and plane view together with STEM images in different zone axes, a precise 3D atomistic model was built. The final nanosail geometry was found to vary slightly depending on its development stage (Figure 2a−d and Supporting Figure S7), but all nanosails were characterized by several common features, discussed below. Similarities among nanowires and nanosails cannot be neglected, and, indeed, as well as growing along the same direction, i.e., $[-111]$, both architectures show a partial common faceting based on {110} planes. For the nanosails, the frontal and back facets always correspond to {110} planes, i.e., (110) and $(-1-10)$, as illustrated in the $[110]$ front view in Figure 2e, but also the vertical side of the nanosail is composed by two different {110} planes (i.e., $(01-1)$ and $(-10-1)$). The bottom lateral side expanding outward and running parallel to the observed twin boundary, belongs to the $(-11-1)$ plane, as well as the upper parallel facet. It is noteworthy that the width of the twinned section is constant along its length. The twin boundary is found to be an orthotwin[63,64] (see Supporting Figure S5), and more details about its position and propagation are given in Supporting Figure S6. Two additional {10l} planes (usually {103}) complete the faceting of the whole morphology. In contrast to the complex higher index facets present where the lateral twin terminates on the top left-hand side of the droplet, the {111} and {110} facets are all atomically flat. A root-mean-square roughness of 3.5 Å has been extracted using atomic force microscopy (AFM).

In terms of the formation mechanism, a few observations should be made prior to describing a growth scenario. First the nanosails retain two small {110} facets (extending directly from the InAs "mast") and two very large {110} facets of the original six {110} planes completing the perfectly hexagonal shape of an InSb nanowire. Second, all nanosails possess the same pure zinc blende crystal structure topped by a $AuIn_2$ alloy particle showing postgrowth perfect strain-free epitaxial relationship with the semiconductor, exactly as InSb nanowires do.[61] Finally the growth conditions leading to the nanosail formation are obviously very close to those favorable for the growth of InSb nanowires since they both grow simultaneously, sometimes within submicron distances from each other, independently of the growth technique (MOVPE or MBE). Therefore, the nanosail formation clearly shares very strong links to the metal-assisted nanowire vapor−liquid−solid growth mechanism. In

the same way, it was shown by several authors that under certain conditions, III−V nanowires can kink to other crystallographic directions,[65,66] including to other polarities[67] or contain internal twins nonperpendicular to their elongation axis.[68,69] In all the above examples it was either demonstrated or at least inferred that the alloyed seed particle was allowed to unpin from its standard {111} growth plane to wet more than one planes (multiple surfaces),[70] including the nanowire sidewalls. Even during standard growth of diamond cubic or zinc blende nanowire crystals, a corner oscillation has been confirmed by in situ growth inside TEMs.[71−73]

Keeping in mind these considerations, Figure 2f illustrates our suggested phenomenological growth scenario to account for the formation of the InSb nanosails. When switching from As to Sb the droplet composition, phases and surface energy balance are changed dramatically. An increase in diameter occurs immediately after the introduction of Sb in the alloyed In(As,Sb) region a few nanometers above the InAs stem.[61] In agreement with a large set of published experimental results,[39,70] the seed droplet is therefore allowed to unpin slightly from its position lying on the (-111) InSb plane to wet the sidewalls. Such a configuration has been shown to allow for new nucleation sites, and if two nuclei originating from two adjacent corners merge together, a grain boundary/twin can easily form. Illustrations of the morphological and structural signatures of this defect are shown in Supporting Figure S6. Once the inclined twin is formed the droplet wets multiple facets: the usual (-111) facet and a new {110} facet or ensemble of connected facets on its outer region (on the left, yellow pointed in Figure 2f). As the growth proceeds along the directions indicated in blue, the droplet will be stretched until the limit of its acceptable deformation in view of its surface tension. Such a dynamic modification of the surface area under the droplet has been described and modeled in detail in the case of twinning superlattices,[74,75] where a further conceptual similarity lies in growth occurring on planes not perpendicular to the growth axis. After reaching its maximal surface tension the droplet will eventually unpin from the inclined lateral facet(s) pointed in yellow in Figure 2f, resulting in the creation of the new facets that narrow the system. The situation shown in Figure 2f likely occurs at a very early stage of the nanosail formation, where its lateral extent does not differ much from that of a nanowire diameter. These sets of facets ({103} in the 3D model shown in Figure 2e will depend on growth kinetics and adapt accordingly. As growth proceeds under the droplet, it may become more favorable for the droplet to stick to the {103}/(-111) triple phase boundary instead at the edge formed by the {110}/(-111) planes depicted on the right-hand side in Figure 2f, leading to the creation of a new {$-11-1$} facet, exactly parallel to the bottom left one. An animated movie on the formation of the nanosails, based on atomic 3D models, can be found online.[76] Now that all of the key facets have been formed, the miniature nanosail grows via both vertical VLS and lateral vapor−solid (VS) epitaxy to create the large surface area nanosheets observed. Future in situ TEM growth studies could refine our understanding of the formation of such an original geometry.[77]

In order to assess the electronic quality of the InSb nanosails, we performed electrical measurements in the van der Pauw geometry, as shown inset of Figure 3a, using a highly conductive n^+ Si substrate covered by 225 nm thermal SiO_2 oxide as a back gate to allow for tuning of the carrier density. This geometry allows direct access to the carrier density
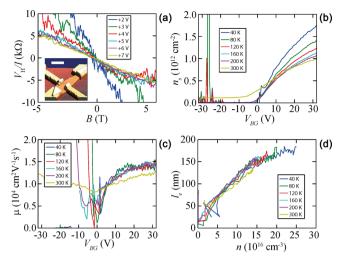
Figure 3. Hall measurements on InSb nanosails. (a) Hall voltage V_H as a function of the magnetic field applied perpendicular to the nanosail surface B for different voltages V_{BG} applied on the back-gate (values given in the legend) at a temperature of 2.1 K. Inset: AFM image of the four-terminal nanosail device (scale bar 500 nm). (b) Sheet electron density n_s as deduced from the Hall measurements using the single carrier model as a function of the back-gate voltage V_{BG} and for different temperatures (values given in the legend). (c) Electron mobility μ as a function of the back-gate voltage V_{BG}. The mobility is calculated from the sheet resistance measured in the van der Pauw configuration and from the electron sheet density presented in panel c. (d) Elastic mean free path l_e as a function of the bulk carrier density n assuming a homogeneous carrier distribution over the 70 nm thickness of the nanosail.

shows the Hall voltage measured as a function of the magnetic field applied perpendicular to the nanosail surface. It follows the expected linear dependence with a negative sign corresponding to electrons. In the following the Hall voltage has been measured at +0.5 T and −0.5 T as a function of the gate voltage and temperature.

At high temperature, the dependence of the Hall voltage on the back gate voltage is nonmonotonous, which is the signature of both electron and hole transport in a low band gap material (see Supporting Information, Figure S8). At lower temperature and positive gate voltage, only electrons participate in carrier transport, and we can therefore apply a single carrier model to determine the sheet electron density n_s, which is plotted as a function of the back gate voltage for different temperatures in Figure 3b. At low temperature, the carrier density shows a threshold and linear variation for a limited range of gate voltages. A fit of the linear region (gate voltage range from +5 to +10 V) at 40 K gives a slope of $(1.36 \pm 0.13) \times 10^{-4}$ C·cm^{-2} and a threshold voltage of $V_T = 0.3 \pm 0.5$ V. The slope is close to the expected value of 1.5×10^{-4} C·cm^{-2} calculated from a plane capacitor model with the dielectric thickness of 225 nm.

We have measured the conductivity σ as a function of gate voltage and temperature using the van der Pauw method[78] (see Supporting Information, Section SF). Similar to the Hall voltage, the conductivity at high temperature is a non-monotonous function of the gate voltage due to mixed electron and hole transport. At positive gate voltage, however, the conductivity is dominated by electron transport due to the low mobility and density of holes. The electron mobility extracted in the single-carrier model is plotted as a function of the gate voltage for different temperatures in Figure 3c. At room-temperature we find the mobility in our 70 nm-thick InSb nanosails to be 1.25×10^4 cm^2·V^{-1}·s^{-1}, a value less than that of

through the Hall effect, and to the intrinsic conductivity and carrier mobility through four-point measurements. Figure 3a
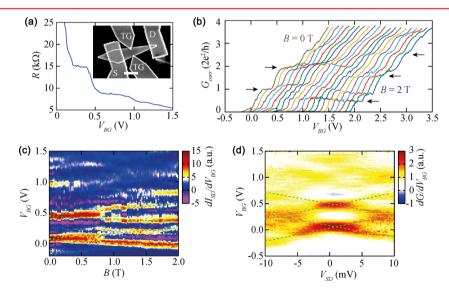

Figure 4. Top-gated quantum point contact to an InSb nanosail. (a) Two-point source−drain resistance of the device as a function of the back-gate voltage V_{BG} for a fixed voltage applied to the top-gates $V_{TG} = +0.68$ V and measured at $T = 6$ K. Inset: image of the top-gated quantum point contact device showing source and drain contacts, and two top gates electrically isolated from the nanosail by 10 nm of HfO$_2$ deposited by atomic layer deposition. (b) Corrected conductance of the device obtained after removing a 2 kΩ series resistance from the two-terminal resistance, corresponding to the contact resistance (see main text), as a function of the back-gate voltage and varying the parallel magnetic field in steps of 0.1 T from 0 to 2 T. The measurement has been performed at $T = 6$ K, and the curves have been laterally shifted by 0.1 V for clarity. The arrows emphasize the steps corresponding to conductance quantization. (c) Color map of $G = dI_{SD}/dV_{BG}$ as a function of the parallel magnetic field and the back-gate voltage emphasizing the conductance steps. The green dashed lines show the splitting of the two first conductance steps measured at $T = 2.1$ K. (d) Color-map of dG/dV_{BG} as a function of the source-drain bias voltage V_{SD} and the back-gate voltage V_{BG} for $V_{TG} = +0.68$ V and $T = 6$ K. The green dashed lines show the edge of the conduction steps.

bulk InSb (7.7×10^4 cm^2·V^{-1}·s^{-1}), but four times larger than 70 nm-thick InSb layers grown on GaAs, and equal to that of 300 nm thick InSb layers.[79,80] This improvement relative to the best values for an InSb layer of similar thickness may be attributed to the absence of strain and dislocations that are inherent to the growth on substrate with large lattice mismatch and demonstrates the significant potential of the nanosail geometry in realizing planar devices.

The mobility is weakly dependent on temperature (see Supporting Information SF.3) and is therefore most probably limited by defect scattering. Due to the absence of structural defects in the nanosail (apart from the single twin as discussed above), we attribute the origin of the scattering to defects close to the InSb surface, either traps in the SiO$_2$ dielectrics, at the SiO$_2$/InSb interface or the top surface.[22] We have also deduced the electron mean free path $l_e = v_F \tau_e$ from the average scattering time $\tau_e = m^* \mu / e$, and the 3D Fermi velocity $v_F = \hbar k_F / m^* = (\hbar/m^*)(3\pi^2 n)^{1/3}$, where n is the electron density. l_e is plotted as a function of n for different temperatures in Figure 3d. That the mobility shows a weak temperature dependence suggests a dominant scattering mechanism other than phonon scattering. Previous work has shown passivation to improve the mobility and mean-free path of nanostructures.[81−83] The relatively large values of l_e found here holds realistic promise for the realization of ballistic transport in future nanosail devices.

In order to test the possibility of realizing ballistic quantum devices from our InSb nanosails, we have fabricated a constriction on a nanosail by depositing two top gates as shown in the inset of Figure 4a. Such a constriction, also known as quantum point contact,[55,56] is expected to lead to quasi-1D electronic transport. We emphasize here that such quasi-1D transport was expected in InSb nanowires, but was only demonstrated at high magnetic field because backscattering at the contacts leads to a destruction of the signatures of 1D transport.[57] Up until now 1D transport in InSb was only demonstrated in 2D electron gases formed in InSb hetero-structures[84] or in InSb nanowires in the presence of an in-plane magnetic field.[57]

The device with top gates showed a strong increase in resistance compared to devices without top gates at zero applied top-gate voltage, which is presumably due to a depletion of the nanosail below the top gates. We further observed that the resistance did not significantly vary with application of top-gate voltage, giving further indication of this total depletion.

The conductance of a quasi-1D constriction is expected to be tuned either by changing the width W of the constriction or by changing the electron wave vector by changing the electron density. In the following we have chosen to tune the carrier density in the constriction by using the back gate instead of tuning the width of the constriction by using the top gate voltage due to instabilities appearing when tuning the top gate, probably due to traps in the dielectric layer.

The two-terminal resistance of the top-gated device is shown as a function of the back-gate voltage for a fixed top-gate voltage $V_{TG} = +0.68$ V in Figure 4a. This curve, obtained at zero magnetic field, clearly shows two plateaux at about 15 kΩ (instead of $h/2e^2 = 12.9$ kΩ) and 8.5 kΩ (instead of $h/4e^2 = 6.5$ kΩ), respectively. For quasi-1D electronic transport at zero magnetic field such plateaux are expected as $h/2e^2 = 12.9$ kΩ and $h/4e^2 = 6.5$ kΩ. We attribute the constant difference to a contact series resistance of about 2 kΩ, as well as the resistance of the nanosail outside the constriction. This resistance is

compatible with the two-terminal resistance obtained in a device with no top gate (such as the one investigated in Figure 3). In order to emphasize further the quantification of the conductance in units of $2e^2/h$, as expected for a quantum point contact, we have plotted the two-terminal conductance corrected by the series resistance of 2 kΩ in Figure 4b. Here a magnetic field parallel to the plane of the nanosail is applied in order to split the 1D subbands. We see in this plot that the two plateaux at $2e^2/h$ and $4e^2/h$ disappear at a magnetic field of 2 T and give rise to plateaux at e^2/h, $3e^2/h$, and $5e^2/h$. Such behavior can be explain by the splitting of the 1D sub-bands as a function of the magnetic field and further confirms that the plateaux are related to 1D transport.

We also investigated the splitting of the 1D sub-bands quantitatively as a function of applied magnetic field. In Figure 4c, we plot the differential conductance $G = dI_{SD}/dV_{BG}$ in order to emphasize the edges of the plateaux. In this plot we clearly observe the splitting of the two first sub-bands. This splitting should occur at a rate of $g^* \mu_B B$. In our case the splitting is 0.146 V/T for both sub-bands. In order to determine the lever arm of the back-gate (the change in Fermi energy as a function of the back-gate voltage), we have measured the nonlinear conductance, i.e., the change in the conductance as a function of the source−drain bias voltage. We see in Figure 4d that the edges of the plateaux split at finite source-drain bias voltage with a rate corresponding to a lever arm of 19.6 meV/V. We then determine a magnetic field splitting of 2.86 meV/T, and a Landé g-factor $|g^*| = 49$, which is close to the expected bulk value of 51.

Finally, we investigated the effect of the top-gate voltage on the level spacing. From nonlinear conductance measurements, we have determined the level spacing between the first two sub-bands at zero magnetic field (Supporting Information section SF.4). The energy for a top-gate voltage $V_{TG} = +0.68$ V is $E_2 - E_1 = 8.7$ meV, corresponding to a constriction of width 80 nm (for an infinite 1D square potential, with an electron effective mass $m^* = 0.014 \times m0$ for electrons in InSb). The level spacing for $V_{TG} = -1$ V is $E_2 - E_1 = 11.1$ meV, corresponding to a constriction of width 70 nm. This dependence further confirms that the quasi-1D channel is formed in-between the two top-gates.

In conclusion we synthesized free-standing, high perform-ance InSb nanostructures with a sheet-like morphology. This novel morphology is characterized by large atomically flat {110} surfaces and results from a single lateral twinning event. We measure a high electron mobility which is promising for both low power nanoelectronics and low temperature transport physics. Demonstration of quantized conductance in a quantum point contact at zero in-plane magnetic field further attests to material quality and the potential for spin−orbit quantum physics applications. We expect that the outlined growth mechanism may be generalized to other materials grown by VLS delivering an easily contacted 2D-like geometry compat-ible with complex radial heterostructures and topological quantum physics experiments.[85] Future work on more advanced device geometries such as suspended nanomembrane devices[86,87] or using dielectric/chemical passivation schemes[81−83,88] could enhance their promising transport figures of merit even further.

ASSOCIATED CONTENT

ⓢ Supporting Information

The Supporting Information is available free of charge on the ACS Publications website at DOI: 10.1021/acs.nano-lett.5b05125.

> Methods, growth, characterization and device processing (Section SA). Statistics on the yield of different morphologies (Section SB, Figures S1−S3). Analysis of the InAs/InSb interface (Section SC, Figure S4). Presence of a unique twin boundary (Section SD, Figures S5 and S6). Faceting of the nanosails (Section SE, Figure S7). Electrical measurements (SF, Section Figures S8−S11) (PDF)

AUTHOR INFORMATION

Corresponding Authors

*E-mail: philippe.caroff@anu.edu.au.
*E-mail: renaud.leturcq@list.lu.
*E-mail: arbiol@icrea.cat.

Present Address

C.R.: SPEC, CEA, CNRS, Université Paris-Saclay, CEA Saclay 91191 Gif-sur-Yvette, France.

Author Contributions

P.C. and R.L. conceived the idea for the research, co-lead the project, and performed respectively the material growth/morphological analyses and most of the device processing/measurements. M.M. performed the complete atomic resolution transmission electron microscopy analysis and built the 3D model as a result of the analysis, under the supervision of and with inputs from J.A., C.M., S.R.P., and P.C., whom altogether discussed and analyzed the growth and structural information. C.R. was involved in the device processing and measurements under the supervision of R.L. All authors commented on the work and provided valuable input throughout the project. P.C. wrote the manuscript with significant contributions from all authors.

Notes

The authors declare no competing financial interest.

REFERENCES

(1) Yan, R.; Gargas, D.; Yang, P. *Nat. Photonics* **2009**, *3* (10), 569−576.

(2) Vitiello, M. S.; Viti, L.; Coquillat, D.; Knap, W.; Ercolani, D.; Sorba, L. *APL Mater.* **2015**, *3* (2), 026104.

(3) Riel, H.; Wernersson, L.-E.; Hong, M.; del Alamo, J. A. *MRS Bull.* **2014**, *39* (08), 668−677.

(4) Wernersson, L.-E. *J. Appl. Phys.* **2015**, *117* (11), 112810.

(5) Frolov, S. M.; Plissard, S. R.; Nadj-Perge, S.; Kouwenhoven, L. P.; Bakkers, E. P. A. M. *MRS Bull.* **2013**, *38* (10), 809−815.

(6) Tomioka, K.; Fukui, T. *Nano Lett.* **2015**, *15* (11), 7189.

(7) Svensson, J.; Dey, A. W.; Jacobsson, D.; Wernersson, L.-E. *Nano Lett.* **2015**, *15*, 7898.

(8) Tomioka, K.; Yoshimura, M.; Fukui, T. *Nature* **2012**, *488* (7410), 189−192.

(9) Lind, E.; Memisevic, E.; Dey, A. W.; Wernersson, L. E. *IEEE J. Electron Devices Soc.* **2015**, *3* (3), 96−102.

(10) Yan, C.; Li, X.; Zhou, K.; Pan, A.; Werner, P.; Mensah, S. L.; Vogel, A. T.; Schmidt, V. *Nano Lett.* **2012**, *12* (4), 1799−1805.

(11) Svensson, J.; Anttu, N.; Vainorius, N.; Borg, B. M.; Wernersson, L.-E. *Nano Lett.* **2013**, *13* (4), 1380−1385.

(12) Duan, X.; Huang, Y.; Agarwal, R.; Lieber, C. M. *Nature* **2003**, *421* (6920), 241−245.

(13) Qian, F.; Li, Y.; Gradecak, S.; Park, H.-G.; Dong, Y.; Ding, Y.; Wang, Z. L.; Lieber, C. M. *Nat. Mater.* **2008**, *7* (9), 701−706.

(14) Chen, R.; Tran, T.-T. D.; Ng, K. W.; Ko, W. S.; Chuang, L. C.; Sedgwick, F. G.; Chang-Hasnain, C. *Nat. Photonics* **2011**, *5* (3), 170−175.

(15) Hicks, L. D.; Dresselhaus, M. S. *Phys. Rev. B: Condens. Matter Mater. Phys.* **1993**, *47* (24), 16631−16634.

(16) Boukai, A. I.; Bunimovich, Y.; Tahir-Kheli, J.; Yu, J.-K.; Goddard Iii, W. A.; Heath, J. R. *Nature* **2008**, *451* (7175), 168−171.

(17) Yamaguchi, S.; Matsumoto, T.; Yamazaki, J.; Kaiwa, N.; Yamamoto, A. *Appl. Phys. Lett.* **2005**, *87* (20), 201902.

(18) Mingo, N. *Appl. Phys. Lett.* **2004**, *84* (14), 2652−2654.

(19) Uryupin, O. N.; Vedernikov, M. V.; Shabaldin, A. A.; Ivanov, Y. V.; Kumzerov, Y. A.; Fokin, A. V. *J. Electron. Mater.* **2009**, *38* (7), 990−993.

(20) Mensch, P.; Karg, S.; Schmidt, V.; Gotsmann, B.; Schmid, H.; Riel, H. *Appl. Phys. Lett.* **2015**, *106* (9), 093101.

(21) Nilsson, H. A.; Caroff, P.; Thelander, C.; Larsson, M.; Wagner, J. B.; Wernersson, L.-E.; Samuelson, L.; Xu, H. Q. *Nano Lett.* **2009**, *9* (9), 3151−3156.

(22) Gül, Ö.; van Woerkom, D. J.; Weperen, I. v.; Car, D.; Plissard, S. R.; Bakkers, E. P. A. M.; Kouwenhoven, L. P. *Nanotechnology* **2015**, *26* (21), 215202.

(23) Nilsson, H. A.; Karlström, O.; Larsson, M.; Caroff, P.; Pedersen, J. N.; Samuelson, L.; Wacker, A.; Wernersson, L. E.; Xu, H. Q. *Phys. Rev. Lett.* **2010**, *104* (18), 186804.

(24) Pribiag, V. S.; Nadj Perge, S.; Frolov, S. M.; van den Berg, J. W. G.; van Weperen, I.; Plissard, S. R.; Bakkers, E. P. A. M.; Kouwenhoven, L. P. *Nat. Nanotechnol.* **2013**, *8* (3), 170−174.

(25) Nadj-Perge, S.; Pribiag, V. S.; van den Berg, J. W. G.; Zuo, K.; Plissard, S. R.; Bakkers, E. P. A. M.; Frolov, S. M.; Kouwenhoven, L. P. *Phys. Rev. Lett.* **2012**, *108* (16), 166801.

(26) van den Berg, J. W. G.; Nadj-Perge, S.; Pribiag, V. S.; Plissard, S. R.; Bakkers, E. P. A. M.; Frolov, S. M.; Kouwenhoven, L. P. *Phys. Rev. Lett.* **2013**, *110* (6), 066806.

(27) Mourik, V.; Zuo, K.; Frolov, S. M.; Plissard, S. R.; Bakkers, E. P. A. M.; Kouwenhoven, L. P. *Science* **2012**, *336* (6084), 1003−1007.

(28) Deng, M. T.; Yu, C. L.; Huang, G. Y.; Larsson, M.; Caroff, P.; Xu, H. Q. *Nano Lett.* **2012**, *12* (12), 6414−6419.

(29) Deng, M. T.; Yu, C. L.; Huang, G. Y.; Larsson, M.; Caroff, P.; Xu, H. Q. *Sci. Rep.* **2014**, *4*, 7261.

(30) Borg, B. M.; Wernersson, L.-E. *Nanotechnology* **2013**, *24* (20), 202001.

(31) Caroff, P.; Messing, M. E.; Borg, B. M.; Dick, K. A.; Deppert, K.; Wernersson, L.-E. *Nanotechnology* **2009**, *20* (49), 495606.

(32) Li, A.; Sibirev, N. V.; Ercolani, D.; Dubrovskii, V. G.; Sorba, L. *Cryst. Growth Des.* **2013**, *13* (2), 878−882.

(33) Plissard, S. R.; Slapak, D. R.; Verheijen, M. A.; Hocevar, M.; Immink, G. W. G.; van Weperen, I.; Nadj-Perge, S.; Frolov, S. M.; Kouwenhoven, L. P.; Bakkers, E. P. A. M. *Nano Lett.* **2012**, *12* (4), 1794−1798.

(34) Park, H. D.; Prokes, S. M.; Twigg, M. E.; Ding, Y.; Wang, Z. L. *J. Cryst. Growth* **2007**, *304* (2), 399−401.

(35) Caroff, P.; Wagner, J. B.; Dick, K. A.; Nilsson, H. A.; Jeppsson, M.; Deppert, K.; Samuelson, L.; Wallenberg, L. R.; Wernersson, L.-E. *Small* **2008**, *4* (7), 878−882.

(36) Ercolani, D.; Rossi, F.; Li, A.; Roddaro, S.; Grillo, V.; Salviati, G.; Beltram, F.; Sorba, L. *Nanotechnology* **2009**, *20* (50), 505605.

(37) Thelander, C.; Caroff, P.; Plissard, S.; Dick, K. A. *Appl. Phys. Lett.* **2012**, *100* (23), 232105.

(38) Gorji Ghalamestani, S.; Ek, M.; Ganjipour, B.; Thelander, C.; Johansson, J.; Caroff, P.; Dick, K. A. *Nano Lett.* **2012**, *12* (9), 4914−4919.

(39) Plissard, S. R.; van Weperen, I.; Car, D.; Verheijen, M. A.; Immink, G. W. G.; Kammhuber, J.; Cornelissen, L. J.; Szombati, D. B.; Geresdi, A.; Frolov, S. M.; Kouwenhoven, L. P.; Bakkers, E. P. A. M. *Nat. Nanotechnol.* **2013**, *8* (11), 859−864.

(40) Car, D.; Wang, J.; Verheijen, M. A.; Bakkers, E. P. A. M.; Plissard, S. R. *Adv. Mater.* **2014**, *26* (28), 4875−4879.

(41) Uccelli, E.; Arbiol, J.; Magen, C.; Krogstrup, P.; Russo-Averchi, E.; Heiss, M.; Mugny, G.; Morier-Genoud, F.; Nygård, J.; Morante, J. R.; Fontcuberta i Morral, A. *Nano Lett.* **2011**, *11* (9), 3827−3832.

(42) Utama, M. I. B.; de la Mata, M.; Magen, C.; Arbiol, J.; Xiong, Q. *Adv. Funct. Mater.* **2013**, *23* (13), 1636−1646.

(43) Dayeh, S. A.; Wang, J.; Li, N.; Huang, J. Y.; Gin, A. V.; Picraux, S. T. *Nano Lett.* **2011**, *11* (10), 4200−4206.

(44) Blömers, C.; Grap, T.; Lepsa, M. I.; Moers, J.; Trellenkamp, S.; Grützmacher, D.; Lüth, H.; SchäPers, T. *Appl. Phys. Lett.* **2012**, *101* (15), 152106.

(45) Storm, K.; Halvardsson, F.; Heurlin, M.; Lindgren, D.; Gustafsson, A.; Wu, P. M.; Monemar, B.; Samuelson, L. *Nat. Nanotechnol.* **2012**, *7* (11), 718−722.

(46) Schelter, J.; Bohr, D.; Trauzettel, B. *Phys. Rev. B: Condens. Matter Mater. Phys.* **2010**, *81* (19), 195441.

(47) Nikoobakht, B.; Li, X. *ACS Nano* **2012**, *6* (3), 1883−1887.

(48) Arab, S.; Chi, C.-Y.; Shi, T.; Wang, Y.; Dapkus, D. P.; Jackson, H. E.; Smith, L. M.; Cronin, S. B. *ACS Nano* **2015**, *9* (2), 1336−1340.

(49) Chang, C.-C.; Chi, C.-Y.; Chen, C.-C.; Huang, N.; Arab, S.; Qiu, J.; Povinelli, M.; Dapkus, P. D.; Cronin, S. *Nano Res.* **2014**, *7* (2), 163−170.

(50) Aagesen, M.; Johnson, E.; Sorensen, C. B.; Mariager, S. O.; Feidenhans'l, R.; Spiecker, E.; Nygard, J.; Lindelof, P. E. *Nat. Nanotechnol.* **2007**, *2* (12), 761−764.

(51) Conesa-Boj, S.; Russo-Averchi, E.; Dalmau-Mallorqui, A.; Trevino, J.; Pecora, E. F.; Forestiere, C.; Handin, A.; Ek, M.; Zweifel, L.; Wallenberg, L. R.; Rüffer, D.; Heiss, M.; Troadec, D.; Dal Negro, L.; Caroff, P.; Fontcuberta i Morral, A. *ACS Nano* **2012**, *6* (12), 10982−10991.

(52) Hsu, C.-W.; Chen, Y.-F.; Su, Y.-K. *Nanoscale Res. Lett.* **2012**, *7* (1), 642.

(53) Chi, C.-Y.; Chang, C.-C.; Hu, S.; Yeh, T.-W.; Cronin, S. B.; Dapkus, P. D. *Nano Lett.* **2013**, *13* (6), 2506−2515.

(54) Tutuncuoglu, G.; de la Mata, M.; Deiana, D.; Potts, H.; Matteini, F.; Arbiol, J.; Fontcuberta i Morral, A. *Nanoscale* **2015**, *7* (46), 19453−19460.

(55) Wharam, D. A.; Thornton, T. J.; Newbury, R.; Pepper, M.; Ahmed, H.; Frost, J. E. F.; Hasko, D. G.; Peacock, D. C.; Ritchie, D. A.; Jones, G. A. C. *J. Phys. C: Solid State Phys.* **1988**, *21* (8), L209.

(56) van Wees, B. J.; van Houten, H.; Beenakker, C. W. J.; Williamson, J. G.; Kouwenhoven, L. P.; van der Marel, D.; Foxon, C. T. *Phys. Rev. Lett.* **1988**, *60* (9), 848−850.

(57) van Weperen, I.; Plissard, S. R.; Bakkers, E. P. A. M.; Frolov, S. M.; Kouwenhoven, L. P. *Nano Lett.* **2013**, *13* (2), 387−391.

(58) Bernal, S.; Botana, F. J.; Calvino, J. J.; López-Cartes, C.; Pérez-Omil, J. A.; Rodríguez-Izquierdo, J. M. *Ultramicroscopy* **1998**, *72* (3−4), 135−164.

(59) Arbiol, J.; Cirera, A.; Peiró, F.; Cornet, A.; Morante, J. R.; Delgado, J. J.; Calvino, J. J. *Appl. Phys. Lett.* **2002**, *80* (2), 329−331.

(60) de la Mata, M.; Magen, C.; Gazquez, J.; Utama, M. I. B.; Heiss, M.; Lopatin, S.; Furtmayr, F.; Fernández-Rojas, C. J.; Peng, B.; Morante, J. R.; Rurali, R.; Eickhoff, M.; Fontcuberta i Morral, A.; Xiong, Q.; Arbiol, J. *Nano Lett.* **2012**, *12* (5), 2579−2586.

(61) de la Mata, M.; Magén, C.; Caroff, P.; Arbiol, J. *Nano Lett.* **2014**, *14* (11), 6614−6620.

(62) Philipose, U.; Sapkota, G.; Salfi, J.; Ruda, H. E. *Semicond. Sci. Technol.* **2010**, *25* (7), 075004.

(63) Cohen, D.; McKernan, S.; Carter, C. B. *Microsc. Microanal.* **1999**, *5* (03), 173−186.

(64) Holt, D. B. *J. Mater. Sci.* **1984**, *19* (2), 439−446.

(65) Wang, J.; Plissard, S. R.; Verheijen, M. A.; Feiner, L.-F.; Cavalli, A.; Bakkers, E. P. A. M. *Nano Lett.* **2013**, *13* (8), 3802−3806.

(66) Fonseka, H. A.; Caroff, P.; Wong-Leung, J.; Ameruddin, A. S.; Tan, H. H.; Jagadish, C. *ACS Nano* **2014**, *8* (7), 6945−6954.

(67) Yuan, X.; Caroff, P.; Wong-Leung, J.; Fu, L.; Tan, H. H.; Jagadish, C. *Adv. Mater.* **2015**, *27* (40), 6096−6103.

(68) Oliveira, D. S.; Tizei, L. H. G.; Li, A.; Vasconcelos, T. L.; Senna, C. A.; Archanjo, B. S.; Ugarte, D.; Cotta, M. A. *Nanoscale* **2015**, *7* (29), 12722−12727.

(69) Yuan, X.; Caroff, P.; Wong-Leung, J.; Tan, H. H.; Jagadish, C. *Nanoscale* **2015**, *7* (11), 4995−5003.

(70) Hocevar, M.; Immink, G.; Verheijen, M.; Akopian, N.; Zwiller, V.; Kouwenhoven, L.; Bakkers, E. *Nat. Commun.* **2012**, *3*, 1266.

(71) Oh, S. H.; Chisholm, M. F.; Kauffmann, Y.; Kaplan, W. D.; Luo, W.; Rühle, M.; Scheu, C. *Science* **2010**, *330* (6003), 489−493.

(72) Gamalski, A. D.; Ducati, C.; Hofmann, S. *J. Phys. Chem. C* **2011**, *115* (11), 4413−4417.

(73) Wen, C. Y.; Tersoff, J.; Hillerich, K.; Reuter, M. C.; Park, J. H.; Kodambaka, S.; Stach, E. A.; Ross, F. M. *Phys. Rev. Lett.* **2011**, *107* (2), 025503.

(74) Algra, R. E.; Verheijen, M. A.; Borgstrom, M. T.; Feiner, L.-F.; Immink, G.; van Enckevort, W. J. P.; Vlieg, E.; Bakkers, E. P. A. M. *Nature* **2008**, *456* (7220), 369−372.

(75) Burgess, T.; Breuer, S.; Caroff, P.; Wong-Leung, J.; Gao, Q.; Hoe Tan, H.; Jagadish, C. *ACS Nano* **2013**, *7* (9), 8105−8114.

(76) http://www.gaen.cat/research/279.

(77) Gamalski, A. D.; Voorhees, P. W.; Ducati, C.; Sharma, R.; Hofmann, S. *Nano Lett.* **2014**, *14* (3), 1288−1292.

(78) Pauw, L. J. v. d. *Philips Technol. Rev.* **1958**, *13*, 220.

(79) Zhang, T.; Clowes, S. K.; Debnath, M.; Bennett, A.; Roberts, C.; Harris, J. J.; Stradling, R. A.; Cohen, L. F.; Lyford, T.; Fewster, P. F. *Appl. Phys. Lett.* **2004**, *84* (22), 4463−4465.

(80) Zhang, T.; Harris, J. J.; Branford, W. R.; Bugoslavsky, Y. V.; Clowes, S. K.; Cohen, L. F.; Husmann, A.; Solin, S. A. *Appl. Phys. Lett.* **2006**, *88* (1), 012110.

(81) Ko, H.; Takei, K.; Kapadia, R.; Chuang, S.; Fang, H.; Leu, P. W.; Ganapathi, K.; Plis, E.; Kim, H. S.; Chen, S.-Y.; Madsen, M.; Ford, A. C.; Chueh, Y.-L.; Krishna, S.; Salahuddin, S.; Javey, A. *Nature* **2010**, *468* (7321), 286−289.

(82) Ford, A. C.; Kumar, S. B.; Kapadia, R.; Guo, J.; Javey, A. *Nano Lett.* **2012**, *12* (3), 1340−1343.

(83) Potts, H.; Friedl, M.; Amaduzzi, F.; Tang, K.; Tütüncüoglu, G.; Matteini, F.; Alarcon Lladó, E.; McIntyre, P. C.; Fontcuberta i Morral, A. *Nano Lett.* **2015**, DOI: 10.1021/acs.nanolett.5b04367.

(84) Goel, N.; Graham, J.; Keay, J. C.; Suzuki, K.; Miyashita, S.; Santos, M. B.; Hirayama, Y. *Phys. E* **2005**, *26* (1−4), 455−459.

(85) Gluschke, J. G.; Leijnse, M.; Ganjipour, B.; Dick, K. A.; Linke, H.; Thelander, C. *ACS Nano* **2015**, *9* (7), 7033−7040.

(86) Bolotin, K. I.; Sikes, K. J.; Jiang, Z.; Klima, M.; Fudenberg, G.; Hone, J.; Kim, P.; Stormer, H. L. *Solid State Commun.* **2008**, *146* (9−10), 351−355.

(87) Schmidt, M.; Schneider, G.; Heyn, C.; Stemmann, A.; Hansen, W. *J. Electron. Mater.* **2012**, *41* (6), 1286−1289.

(88) Suyatin, D. B.; Thelander, C.; Björk, M. T.; Maximov, I.; Samuelson, L. *Nanotechnology* **2007**, *18* (10), 105307.

■ NOTE ADDED IN PROOF

During the reviewing process, we became aware of an independent related work available online on ArXiv (D. Pan et al., http://arxiv.org/abs/1511.06823) which describes silver-catalyszed high mobility InSb nanosheets. This complementary work further highlights the interest and accessibility of the novel III-V crystal shape studied in the present work.